Modeling of dual frequency capacitively coupled plasma sources utilizing a full-wave Maxwell solver: I. Scaling with high frequency

Yang Yang[1,3] **and Mark J Kushner**[2,4]

[1] Iowa State University, Department of Electrical and Computer Engineering, Ames, IA 50011, USA
[2] University of Michigan, Department of Electrical Engineering and Computer Science, 1301 Beal Avenue, Ann Arbor, MI 48109, USA

E-mail: yang_yang@amat.com and mjkush@umich.edu

Abstract

Dual frequency capacitively coupled plasma (DF-CCP) tools for etching and deposition for microelectronics fabrication typically use a high frequency (HF, tens to hundreds of MHz) to sustain the plasma and a low frequency (LF, a few to 10 MHz) for ion acceleration into the wafer. With an increase in both the HF and wafer size, electromagnetic wave effects (i.e. propagation, constructive and destructive interference) can affect the spatial distribution of power deposition and reactive fluxes to the wafer. In this paper, results from a two-dimensional computational investigation of a DF-CCP reactor, incorporating a full-wave solution of Maxwell's equations, are discussed. As in single frequency CCPs, the electron density transitions from edge high to center high with increasing HF. This transition is analyzed by correlating the spatial variation of the phase, magnitude and wavelength of the HF electric field to the spatial variation of the electron energy distributions and ionization sources. This transition is sensitive to the gas mixture, particularly those containing electronegative gases due to the accompany change in conductivity. The consequences of these wave effects on the ion energy distributions incident onto the wafer are also discussed.

(Some figures in this article are in colour only in the electronic version)

1. Introduction

Parallel plate capacitively coupled plasma (CCP) sources are widely used for dry-etching and deposition of materials for microelectronics fabrication. One method of improving the performance of CCP sources is applying multi-frequency radio frequency (rf) sources with the goal of separately controlling ion and radical fluxes, and ion energy distributions to the substrate [1–4]. Typically in a dual frequency capacitively coupled plasma (DF-CCP) reactor, power is applied at a lower frequency to the bottom electrode (a few MHz to 10 MHz) holding the wafer; and higher frequency power is applied to the upper electrode (tens of MHz to hundreds of MHz) often also serving as the shower head. Power at the lower frequency is intended to control the shape of the ion energy and angular distributions (IEADs) to the wafer. Power at the higher frequency is intended to control the production of ions and radicals. (In some variants of DF-CCPs, both frequencies are applied to the lower electrode [4].) Decoupling the two rf sources is desirable to achieve this separate control. With the low frequency (LF) kept at a few MHz, increasing the high frequency (HF) to tens to hundreds of MHz is necessary to functionally separate the two rf sources [5].

DF-CCP reactors were first developed at a time when the wafer size was transitioning from 200 to 300 mm. With increases in the HF and wafer size, and reductions in the effective plasma shortened wavelength, finite wavelength

[3] Present Address: Applied Materials, Inc., 974 E. Arques Ave., Sunnyvale, CA 94085 USA.
[4] Author to whom any correspondence should be addressed.

1

effects became increasingly important in determining the uniformity of the plasma [6]. These effects include constructive and destructive interference and skin effects. For example, voltage applied to the rear of the electrode must propagate around the edges of the electrode to enter the plasma. At this point, the resulting electric field is wave-guided in the sheath at the surface of the electrode. At sufficiently low frequency (large wavelength), the electric field uniformly appears across the sheath. For sufficiently high frequency (short wavelength), constructive interference of the counter-propagating waves from opposite sides of the electrode increases the amplitude of the electric field in the sheath at the center of the electrode. This can produce a center-high plasma density.

Perret *et al* investigated the uniformity of ion fluxes in a large-area square (40 cm × 40 cm) capacitive discharge sustained in argon at 150 mTorr driven at frequencies between 13.56 and 81.36 MHz [7]. Center peaked (meaning the maximum is near the center of the electrode) ion fluxes were observed above 60 MHz with a power deposition of 50 W, an affect attributed to the finite wavelength of the counter-propagating applied electric fields constructively interfering at the center of the reactor. At higher power (170–265 W) and higher plasma densities, the conductivity of the plasma increased sufficiently that the skin depth for electric field penetration became commensurate with the electrode gap. At that point, edge peaked (meaning the maximum is near the edge of the electrode) ion fluxes were observed due to this skin effect with there also likely being a contribution from electrostatic (ES) edge effects that concentrated power there.

Hebner *et al* performed diagnostics of single frequency and DF-CCP reactors operating in argon and driven at frequencies between 10 and 190 MHz [8, 9]. They found that with a grounded lower electrode, the spatial distribution of argon ions transitioned from uniform to center peaked as the excitation frequency was increased on the upper electrode. At 50 mTorr and 60 MHz, they found that with increasing power (300 to 1000 W) the electron density transitioned from being uniform as a function of radius to being center peaked. These trends may be explained by the constructive interference of the plasma shortened wavelength with increasing electron density and conductivity.

Based on an analytic model, Lieberman *et al* developed scaling laws to describe these finite wavelength effects [6]. They found that for a discharge radius of 50 cm, an electrode separation of 4 cm and a sheath width of 2 mm, there is a substantial skin effect for plasma densities higher than 10^{10} cm^{-3}, and there is a substantial standing wave effect for frequencies higher than 70 MHz. Lee *et al* simulated single frequency CCP discharges using the finite element method [10]. Their two-dimensional (2D) continuum model coupled Maxwell's equations (in the frequency domain), fluid plasma equations (in the time domain) and a sheath model. At 80 MHz and 150 mTorr, they found that the plasma density transitioned from center high to edge high with an increase in power from 40 to 190 W, a trend attributed to the decreasing skin depth. At 150 MHz, they predicted a transition in plasma density from edge high at 40 W to center-and-edge high at 160 W,

a trend attributed to decreasing wavelength and constructive interference.

Rauf *et al* numerically investigated the consequences of varying power, inter-electrode gap and gas mixture (Ar, Ar/SF$_6$, Ar/CF$_4$) on plasma properties in CCPs driven at 180 MHz [11]. Their 2D continuum model included Maxwell's equations in the form of scalar and vector potentials. They found that ES effects dominated in electronegative plasmas because the applied rf potential is considerably larger for the same power compared with an electropositive plasma; and that the electron density and the rf current flowing through the discharge are smaller.

In this paper, we build upon these prior works by discussing results from a computational investigation of a DF-CCP reactor with plasmas sustained in Ar and Ar/CF$_4$. Systematic trends for plasma properties, electron energy distributions (EEDs), ion fluxes and IEADs are discussed for a reactor resembling an industrial design. We found that for discharges sustained in Ar, similar to the trends in a single frequency CCP, the electron density transitions from being edge high to center high with increasing HF (from 10 to 150 MHz) [7, 8]. These transitions result from a radial change in the amplitude of the electric field in the sheaths. The shapes of the EEDs near the sheath and in the bulk plasma respond to these changes in electric field as well. Since the sheath thickness (through the change in plasma density) and time variation of the electric field are sensitive to frequency, the IEADs incident onto the wafer become functions of radius. For discharges sustained in Ar/CF$_4$ = 90/10, the electron density also transitions from edge high to middle high (meaning the maximum is at a radius between the center and edge of the electrode) with increasing HF (from 10 to 150 MHz). These trends are due to the coupling of ES edge, skin and finite wavelength effects. The coupling of these effects becomes spatially dependent as the electronegativity, and so plasma conductivity, also has a spatial dependence. This study is extended in part II with an investigation of the scaling of DF-CCPs at HF with pressure, power and gas mixture [12].

The model used in this study is discussed in section 2. Parametric results from our investigation of properties of Ar and Ar/CF$_4$ plasmas sustained in a DF-CCP are presented in sections 3 and 4. Our concluding remarks are in section 5.

2. Description of the model

The model used in this investigation is the 2D Hybrid Plasma Equipment Model (HPEM) which utilizes an electron Monte Carlo simulation (EMCS) to obtain the EEDs of bulk electrons and secondary electrons emitted from surfaces. The model is described in detail in [13].

Briefly, continuity, momentum and energy equations for neutrals and ions; continuity equations for electrons and Maxwell's equations are integrated in time over many hundred rf cycles to obtain a periodic steady state. The resulting electric fields and ion fluxes to surfaces are periodically transferred to the EMCS where the transport of bulk electrons and secondary electrons emitted from surfaces is addressed. Electron transport coefficients, temperatures, impact source

functions and sources of secondary electron current obtained from the EMCS are returned to the fluid model. The process is iterated to convergence. During the last iteration, the converged electric fields and source functions for ions and neutrals are recorded as a function of position and phase in the rf cycle. With these values, the energy and angular distributions of ions and neutrals incident on the substrate are obtained using the Plasma Chemistry Monte Carlo Module described in detail in [14]. Powers are separately specified for the LF and HF sources, and the applied voltages are adjusted to deliver those powers. The powers are computed from $P = (1/\Delta t) \int V I \cdot \Delta t$, where V and I are the voltage and total current at the surface of the electrode and Δt is the rf period.

A self-bias voltage is computed for an electrode by identifying metal surfaces that are connected to the powered side of the voltage source through a blocking capacitor and identifying metal surfaces connected to ground. Currents (conduction and displacement) flowing to each sets of surfaces are integrated over the rf cycle and the resulting charges are placed on the blocking capacitor, thereby charging it to the dc bias.

As an improvement to the previously described model, a solution of Maxwell's equations is integrated into the plasma hydrodynamics modules of the HPEM. This enables the simulation of the inductive effects that result from wave penetration at HF into plasmas and finite wavelength effects, in addition to the ES effects generally accounted for when solving Poisson's equation. This solution was implemented in the time domain so that coupling between frequencies could be explicitly addressed as well as enabling intra-rf period feedback between plasma transport and the electromagnetic (EM) wave.

A full-wave Maxwell solver is computationally challenging due to the coupling between EM and ES fields, the latter of which are responsible for the formation of the sheath. In principle, these fields are from different sources. EM fields are generated by waves launched into the reactor from the cable attached to the power supply which for all practical purposes acts as an antenna. ES fields are produced by charges. As such, we separately solved for the EM and ES fields and summed the fields for plasma transport. In doing so, self-consistent boundary conditions (BCs) can be defined with the capability of addressing multiple rf sources in the time domain.

2.1. EM solution ($\vec{E}_M$)

We implemented the EM solution in a cylindrical geometry though the method is more general. We assumed that rf power is fed into the DF-CCP reactor by coaxial cables which can be at arbitrary locations. In our geometry, the wave propagates in the coaxial cable in a TEM mode, which only has components of E_r (radial electric field) when the cable is connected to horizontal surfaces, E_z (axial electric field) when the cable is connected to vertical surfaces, and B_θ (azimuthal magnetic field). As such, azimuthally symmetric TM modes are excited in the reactor [15]. So in 2D cylindrical coordinates, Faraday's law and Ampere's law can be written as

$$\frac{\partial E_r}{\partial z} - \frac{\partial E_z}{\partial r} = -\frac{\partial B_\theta}{\partial t}, \tag{1}$$

$$-\frac{\partial B_\theta}{\partial z} = \mu J_r + \varepsilon\mu\frac{\partial E_r}{\partial t}, \tag{2}$$

$$\frac{1}{r}\frac{\partial(r B_\theta)}{\partial r} = \mu J_z + \varepsilon\mu\frac{\partial E_z}{\partial t}, \tag{3}$$

where J_r and J_z are the radial and axial components of the conduction current, μ is the permeability and ε is the permittivity. Equations (1)–(3) were discretized on a staggered mesh and solved using the finite difference time domain (FDTD) techniques [15–17]. The spatial locations of E_r, E_z and B_θ were chosen to provide central spatial differencing. B_θ is computed at the centers of mesh cells. Electric fields are calculated at locations shifted by half a mesh cell in the radial direction for E_z and in the axial direction for E_r. The ES potential and plasma densities are computed at the vertices of the mesh cells. Radial and axial fluxes of all species are computed at the locations of E_r and E_z, respectively. To avoid a singularity in cylindrical coordinates, equation (3) is solved using the integral form at $r = 0$.

The rf electric field is launched into the DF-CCP reactor where the power cable is connected. The wave is therefore generated by a source electric field

$$E(t) = V(t)/d \tag{4}$$

which is used as a BC in our model. $V(t)$ is the time dependent voltage drop between the center conductor and the ground shield of the cable connected to the reactor, and d is the spacing between them. For BCs on a metal surface, the tangential component of the electric field is zero. A first order Mur's absorbing BC (a one-way wave equation for extrapolation of electric fields tangential to the boundary of interest) is applied at pump ports or dielectric windows to represent open boundaries [18]. In this staggered mesh and with the Crank–Nicholson scheme, Mur's absorbing BC is accurate to second order in both the time and space integration.

If we explicitly solve equations (1)–(3), the time step is limited by the Courant condition. To allow for larger time steps, the unconditionally stable Crank–Nicholson scheme was employed [19]. The current terms in equations (2) and (3) contain contributions from electrons and ions, which are proportional to electron or ion flux. The electron flux is computed using a drift-diffusion approximation which contains the term $\sigma\vec{E}$, where σ is the electron conductivity. Computational implicitness is therefore achieved by the dependence of the electron flux on the electric field through this term. (The same technique is used for currents through non-metal materials.) Ion fluxes are given by the solution of their respective ion momentum equations from the previous time step and are held constant during the solution of equations (1)–(3). Since the time steps are typically small fractions of the rf cycle (for example, 0.005 for a frequency of 150 MHz) there is little change in ion fluxes during a single time step.

We found that large gradients in plasma conductivity from the sheath to the bulk plasma produce large mesh-point-to-mesh-point changes in electric fields. These changes tend to cause numerical instabilities and artificial resonances. In principle this can be addressed using a finer mesh for the

entire calculation. We found, however, that only the mesh upon which the EM quantities are solved needs to be finer. So to make the task less computationally expensive, the mesh used for plasma properties was subdivided when solving equations (1)–(3). Our typical numerical mesh spacing was 0.1 cm in the axial direction and 0.3 cm in the radial direction. Subdividing the cells in the axial direction by a factor of 2 was enough to prevent numerical instabilities and eliminate artificial resonances.
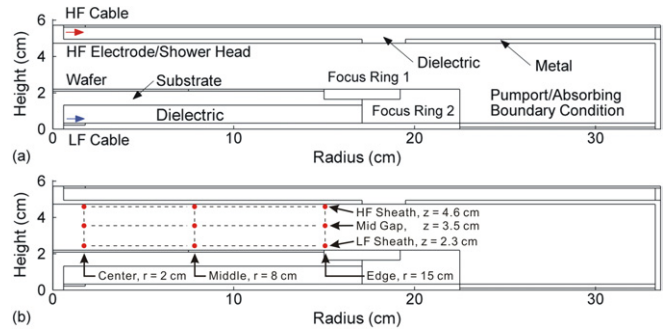
Equations (1)–(3) were solved on the subdivided mesh using sparse matrix techniques. Fields were then interpolated back to the original mesh for use in transport equations and other modules. We also found that for the conditions in this work, the magnitude of B_θ in the plasma is small (< 0.2 G). To save computational time, B_θ was not included in the transport equations for charged particles. We verified that not including B_θ generally leads to a less than 5% change in the final results.

2.2. ES solution ($\vec{E}_S$)

In principle, Poisson's equation is already included in the model when equations (1)–(3) are solved along with the charged species continuity equations for current densities. However, we will not be able to resolve the electric field due to the ES charges sitting on the boundaries and the blocking capacitor without explicitly solving Poisson's equation. It is also difficult to self-consistently define both EM and ES BCs in the absence of Poisson's equation. In our model, Poisson's equation is solved using the semi-implicit technique described in [13]. Potentials, evaluated at the future time, are then used to explicitly integrate charged densities and fluxes. The semi-implicitness is achieved through the prediction of the accumulated charges on surfaces and in the bulk plasma at the future time by numerically evaluating Jacobian elements (perturbing the potentials by a small fraction and computing the change in electron fluxes). Ion fluxes are given by the solution of their ion momentum equations from the previous time step with a prediction for the change in their fluxes during the current time step based on their recent time history. Note that BCs for solution of $\vec{E}_S$ on the powered electrode are not the applied rf voltages as they have already been accounted for in the EM solution. Here, the BCs on the powered electrodes are either the self-developed dc bias or any applied dc voltages.

The EM and ES solutions are then summed to provide the electric field for plasma transport, $\vec{E} = \vec{E}_M + \vec{E}_S$. This total electric field is then used for acceleration of charged particles. Since the model is written in a modular fashion, the rest of the code is unaffected by this choice of field other than substituting this value for the electric field wherever they appear in transport equations for charged particles.

The reaction mechanisms for the Ar and Ar/CF$_4$ mixtures used in this study are discussed in [20]. For Ar, the species included in the model are Ar(3s), Ar(4s) and Ar$^+$. The Ar(4s) is an effective state having a finite lifetime to account for the partial trapping of resonant levels in that manifold. With CF$_4$, the additional species included in the model are CF$_4$, CF$_3$, CF$_2$, CF, F, F$_2$, C$_2$F$_3$, C$_2$F$_4$, C$_2$F$_6$, CF$_3^+$, CF$_2^+$, CF$^+$, F$^+$, CF$_3^-$ and F$^-$. For the operating conditions in this work, the dominant ions and neutral radicals are Ar$^+$, CF$_3^+$, F$^-$, CF$_2$ and CF.

Figure 1. Properties of the DF-CCP reactor. (*a*) Schematic showing the wafer on a substrate powered at LF surrounded by dielectric focus rings. The showerhead is powered at HF and is also surrounded by a dielectric. The HF and LF electric fields are launched into the reactor at the cable connections. (*b*) The radial and axial positions where EEDs will be plotted.

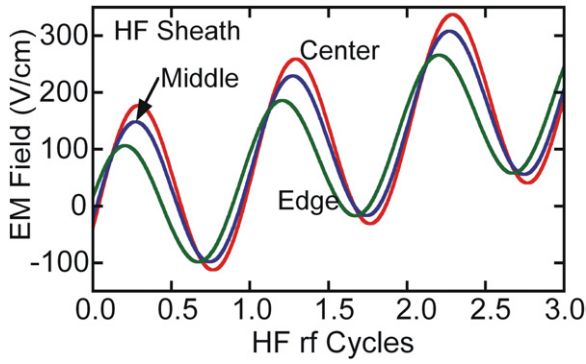## 3. Plasma properties of DF-CCP reactors sustained in Ar

The model reactor used in this study is schematically shown in figure 1. A metal substrate powered at the LF (10 MHz) through a blocking capacitor is the lower electrode. A conductive Si wafer ($\sigma = 0.01$ Ω^{-1} cm^{-1}), 30 cm in diameter, sits in electrical contact with the substrate which is surrounded by a Si ring (focus ring 1, $\varepsilon/\varepsilon_0 = 12.5$, $\sigma = 10^{-6}$ Ω^{-1} cm^{-1}) and a dielectric focus ring (focus ring 2, $\varepsilon/\varepsilon_0 = 8.5$, $\sigma = 10^{-8}$ Ω^{-1} cm^{-1}). The substrate is also encased in a dielectric having $\varepsilon/\varepsilon_0 = 4.0$. Gas is injected through a shower head 34 cm in diameter that also serves as the HF electrode. The HF electrode is surrounded by a dielectric having $\varepsilon/\varepsilon_0 = 4.0$. All other surfaces in the reactor are grounded metal including the annular pump port.

The base case operating conditions are 50 mTorr of Ar with the LF held constant at 10 MHz, delivering a power of 300 W. The HF was varied from 10 to 150 MHz with a constant power of 300 W. The HF and LF powers were fed into the reactor on the axis at the top and bottom of the reactor, So the EM waves producing the plasma are launched into the reactor where the power cables are connected, propagate through the surrounding dielectrics and around the metal electrodes, and then enter into the plasma. In this HF regime, plasma properties are sensitive to the details of the design of the reactor, such as where the rf power is applied and the path the EM wave follows from the power cable to the plasma. We acknowledge the details of our observations and conclusions may change in a different reactor, though we believe the trends are general to this class of reactor.

In this paper the terms LF and HF refer to the LF, here 10 MHz, applied to the bottom electrode and the HF, 10–150 MHz, applied to the top electrode. These terms should not be confused with definitions often found in the electromagnetics literature where LF refers to 30–300 kHz (the kilometer band) and HF refers to 3–30 MHz (the decameter band).

The propagation of the HF EM wave in the reactor is partly illustrated in figure 2, where the EM field is plotted in the time domain (during 3 HF rf cycles at 150 MHz) at
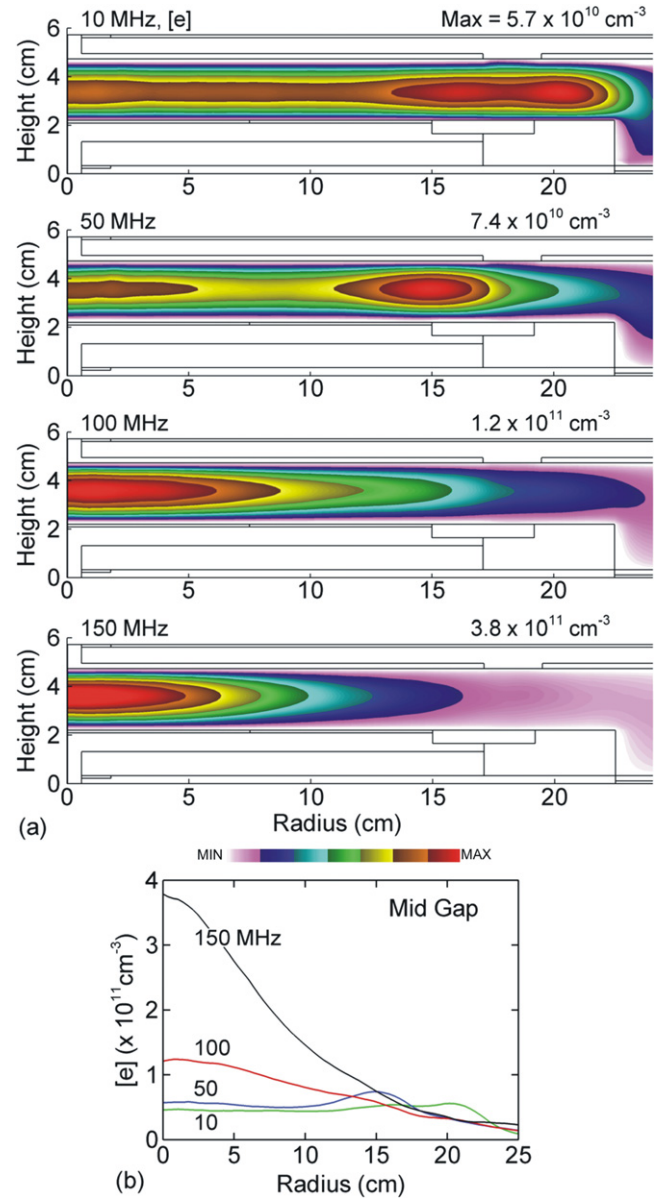
Figure 2. The amplitude of the EM field in the HF sheath at different radial locations over three HF rf cycles (center, $r = 1$ cm; middle, $r = 8$ cm; edge, $r = 16$ cm).

different radial locations along the HF sheath. As the HF wave propagates from the edge of the electrode toward the center of the reactor along the HF sheath, there is a phase change corresponding to the propagation delay. The magnitude of the electric field increases due to the constructive interference of the counter-propagating waves from opposite edges of the electrodes approaching the center of the reactor. Note the electric field becomes increasingly positively biased because the time plotted is during the first half of the LF anodic cycle.

3.1. Electron density and EM fields

The electron density ([e]) is shown in figure 3 for LF = 10 MHz (300 W) and HF = 10–150 MHz (300 W). These quantities have been averaged over the longer LF cycle. (The plasma is fairly well confined between the electrodes and does not appreciably extend into the volume of the reactor above the pump port. Therefore, only the region of the reactor directly above the substrate is shown in this and following figures.) The reactor averaged electron density increases with increasing HF (1.4×10^{10} cm^{-3} at 10 MHz to 2.9×10^{11} cm^{-3} at 150 MHz), a consequence of the increased fraction of power dissipated in electron heating as the HF increases. The radial profile of [e] also varies with the HF. The electron density transitions from being nearly flat as a function of radius at HF = 10 MHz to edge peaked at 50 MHz (with a small peak in the center) and to center peaked at 100 and 150 MHz. This general trend agrees with the experimental results reported in [8], albeit absent the LF power.

With increasing the HF from 10 to 150 MHz, the electric field launched by the HF source transitions from being largely ES to largely EM. (For brevity, and if not otherwise noted, references to the wave amplitude, phase, skin depth and wavelength are for the HF source.) This transition is partly indicated by the increasing phase change of the axial EM field in the HF sheath with increasing HF, as shown in figure 4(a). Note that our model computes the EM field in the time domain. A Fourier transform is performed at the HF to obtain the spatially dependent phase and magnitude of the first harmonic. At all HF, the phase change per centimeter diminishes toward the center of the reactor, which indicates a transition from a traveling wave to a standing wave due to
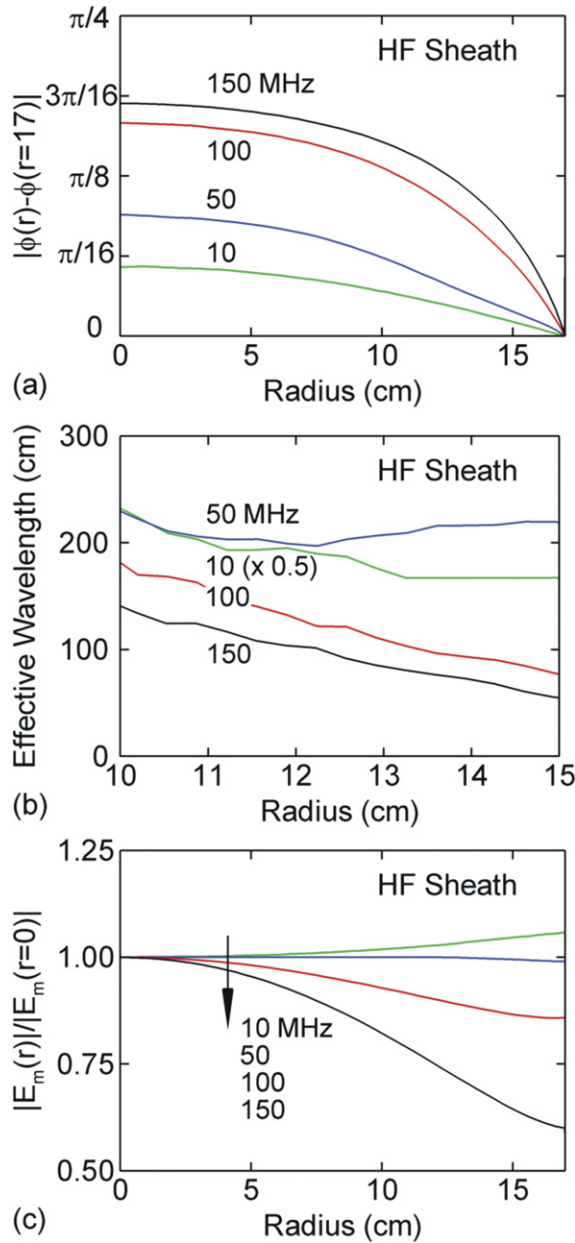

Figure 3. Time averaged electron density ([e]) for the base case conditions (Ar, 50 mTorr, $P_{HF} = P_{LF} = 300$ W, LF = 10 MHz). (a) HF = 10, 50, 100, 150 MHz and (b) radial [e] profile at the mid-gap ($z = 3.5$ cm). The maximum value or range of values in each frame is noted. The electron density is plotted on a linear scale. The electron density transitions from being flat at HF = 10 MHz, to edge peaked at 50 MHz, to center peaked at 100 and 150 MHz.

constructive interference. Standing waves are formed when two waves having the same frequency propagate in opposite directions. So even at 10 MHz, a standing wave is formed at the center of the reactor. This standing wave does not, however, produce significant non-uniformities in the plasma as its wavelength is much longer than the radius of the electrode.

The wave propagating inward along the HF sheath is basically a surface wave and a simple analytical solution of its effective wavelength is not available. Its wavelength was estimated using

$$\lambda_{\text{eff}} = \frac{2\pi}{(\partial \phi / \partial r)}, \quad (5)$$

Figure 4. EM properties for the base case conditions (Ar, 50 mTorr, $P_{HF} = P_{LF} = 300$ W, LF = 10 MHz) and HF = 10–150 MHz. (a) Relative phase (with respect to the edge of the HF electrode) along the HF sheath, (b) plasma effective wavelength along the HF sheath and (c) magnitude of the HF field along the HF sheath (normalized by the magnitude at the center of the reactor). The HF field is highly peaked in the center at 150 MHz due to constructive interference.
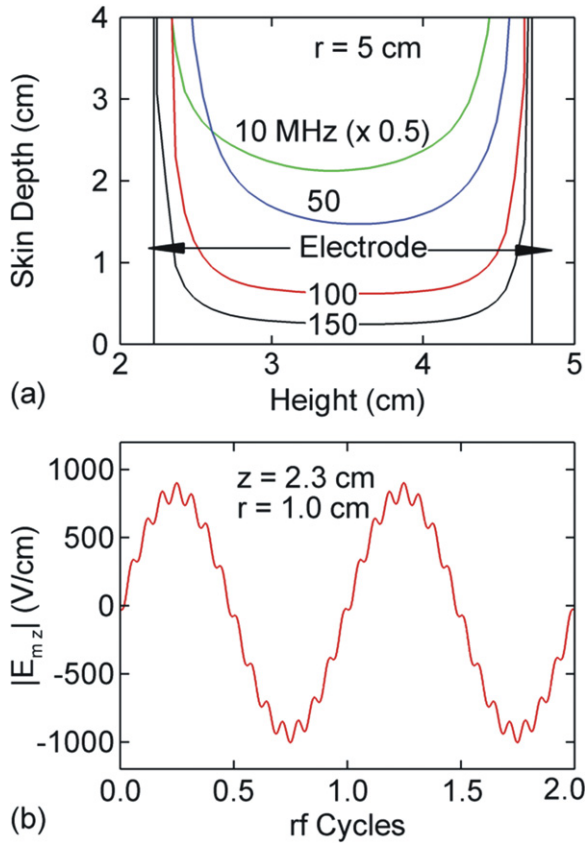
where λ_{eff} is the plasma effective wavelength and $\partial\phi/\partial r$ is the derivative of the phase change in the radial direction. The estimated wavelengths in the HF sheath as a function of radius (from 10 to 15 cm) are shown in figure 4(b) for HF = 10–150 MHz. The wavelength decreases with increasing HF and the half-wavelength becomes commensurate to the electrode diameter for HF > 100 MHz. The increase in wavelength with decreasing radius is somewhat artificial as the phase change diminishes toward the center of the reactor. So the estimated wavelength near the periphery of the upper electrode is most indicative.

As the wavelength decreases with increasing HF, the EM field in the HF sheath becomes increasingly center peaked due to constructive interference of the counter-propagating waves. This trend is shown in figure 4(c), where the magnitude of the HF electric field in the sheath is plotted as a function of radius for HF = 10–150 MHz. The fields are normalized by their values at $r = 0$ to emphasize their radial variations. At 10 MHz, the EM field is largely uniform with higher values near the periphery of the HF electrode resulting from ES edge enhancement. As the HF increases, the wavelength decreases and the magnitude of the electric field near the edge of the electrode decreases relative to the center. This decrease in field occurs as the zero node at a quarter wavelength approaches the edge of the electrode as the wavelength decreases. When exceeding 100 MHz, the EM finite wavelength effect (that is, constructive interference) dominates over edge effects (electric field enhancement or skin effects) and the electric field becomes center peaked. At 150 MHz, the amplitude of the EM field is larger by a factor of 1.7 from the edge to the center of the electrode. This increase in electric field, which is responsible for the center peaked electron density at 150 MHz, originates from the shortening of the wavelength. As such, it may be more accurate to refer to a center high plasma density at HF as being produced by a finite wavelength effect instead of a standing wave effect, as standing waves are produced even at 10 MHz.

The EM skin depth also decreases with increasing HF. The skin depth as a function of height at $r = 5$ cm for HF = 10–150 MHz is shown in figure 5(a). We calculated the skin depth according to [21]

$$\delta = \frac{1}{\omega\sqrt{\mu\varepsilon}\left\{\frac{1}{2}\left[\sqrt{1+(\sigma/\omega\varepsilon)^2}-1\right]\right\}^{1/2}}, \qquad (6)$$

where $\omega = 2\pi f$ is the angular frequency and σ the plasma conductivity. Note that this skin depth corresponds to the evanescent wave that propagates into the bulk plasma, not to the surface wave that propagates along the HF sheath. Exceeding 100 MHz, the skin depth in the bulk plasma is less than 1 cm, which is shorter than half the electrode separation. Note that the skin depth is calculated at $r = 5$ cm where the electron density is relatively high for HF of 100 and 150 MHz. The skin depth in the low electron density region (for example, near the edge of the HF electrode) is commensurate with the electrode separation. Therefore, even at 150 MHz the HF wave can penetrate across the gap and propagate into the LF sheath at the edge of the reactor. The wave then propagates along the LF sheath toward the center of the reactor and so modulates the electric field in the LF sheath. This HF modulation is shown in figure 5(b), where the axial EM field in the LF sheath at $r = 1$ cm is plotted in the time domain. We note that the modulation of the LF sheath at the HF occurs even if an ES approximation is used (that is, solving only Poisson's equation). This modulation is ultimately a consequence of current at the HF passing through the LF sheath, which then modulates its potential. So models which account for current continuity at all frequencies, as would an ES approximation, will capture

Figure 5. EM properties for the base case conditions (Ar, 50 mTorr, $P_{HF} = P_{LF} = 300$ W, LF = 10 MHz) and HF = 10–150 MHz. (*a*) Skin depth as a function of height at $r = 5$ cm and (*b*) the axial EM field in the LF sheath at $r = 1$ cm (in the time domain).

this modulation, though the phase of the modulation may be different.

Subtleties of the design of the reactor are important in these scalings. For example, in the model reactor, the HF electrode is separated from ground by a 2.5 cm dielectric gap. This spacing likely intensifies edge effects compared with a larger gap and in part prolongs the edge-high plasma density as the frequency is increased.

3.2. Inductive electric fields and power deposition

The HF wave propagates into the bulk plasma from the edge of the HF electrode, and so the absorption of the wave by the plasma is usually strongest in the axial direction (into the bulk plasma) near the edge of the HF electrode. The axial gradient of the magnetic field therefore peaks near the edge of the HF electrode, which in turn, produces a peak in the radial HF field. This radial HF field tends to enhance the power deposition near the edge of the electrode thereby increasing the local plasma density. This radial field and its electron heating effects are usually referred to as the inductive field and inductive heating [6, 8–11].
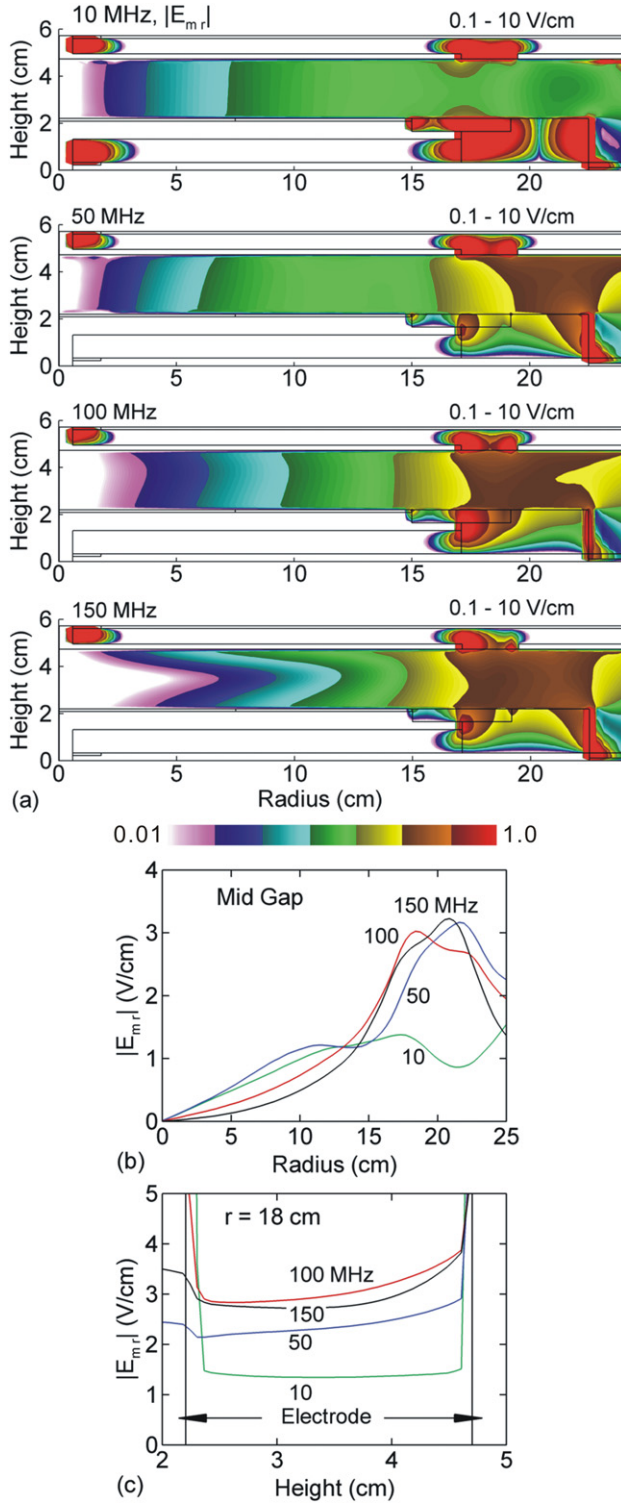
The magnitude of the radial HF field (first harmonic amplitude, E_{mr}) is shown in figure 6 for HF = 10–150 MHz. (In order to resolve E_{mr} in the bulk plasma, the dynamic range of the color bar in figure 6 does not resolve the large values

of E_{mr} in the dielectrics near the edge of the electrode and at the HF power cable.) As expected, E_{mr} peaks near the edge of the electrode at all HF. The magnitude of E_{mr} is not a linear function of HF, as the electron density profiles change with the HF and, as a result, so do the absorption, reflection and diffraction patterns of the HF wave. The axial profile of E_{mr} is flat in the bulk plasma at the edge of the upper electrode for HF of 10 and 50 MHz owing to the large skin depth at those frequencies. As the HF increases, E_{mr} tends to flow along the plasma–sheath edge, producing a minimum in the bulk plasma [6]. However, even at 150 MHz, E_{mr} is relatively flat as a function of height near the edge of the HF electrode where the electron density is low and the local skin depth is commensurate with the electrode separation. In the bulk plasma near the edge of the HF electrode, the magnitudes of E_{mr} (1–4 V cm^{-1} from 10 to 150 MHz) are much larger than those of the axial HF field (0.06–0.3 V cm^{-1} from 10 to 150 MHz). This results from the radial gradient of the HF magnetic field being much smaller than the axial gradient due to the radially traveling surface wave.

The contribution of E_{mr} to the bulk power deposition near the edges of the electrodes is partly shown in figure 7, where the total power deposition is plotted for HF = 10–150 MHz. The total power deposition is obtained by a LF cycle average of the instantaneous power, $P_{tot}(\vec{r}) = (1/\Delta t) \int \vec{E} \cdot \vec{J} \Delta t$, where Δt is the LF period. With increasing HF, the power deposition in the middle of the electrode gap near the edge increases, indicating an increasing skin effect. The maximum in the power deposition is, however, in the sheath and this maximum moves toward the center of the reactor with increasing frequency as a result of the surface wave effect (figure 7(*c*)) [6]. The skin effect, which increases power deposition in the bulk plasma, does not produce a maximum in electron density at the edge of the electrode at HF $\geqslant$ 100 MHz due to power deposition being dominated by the surface wave.
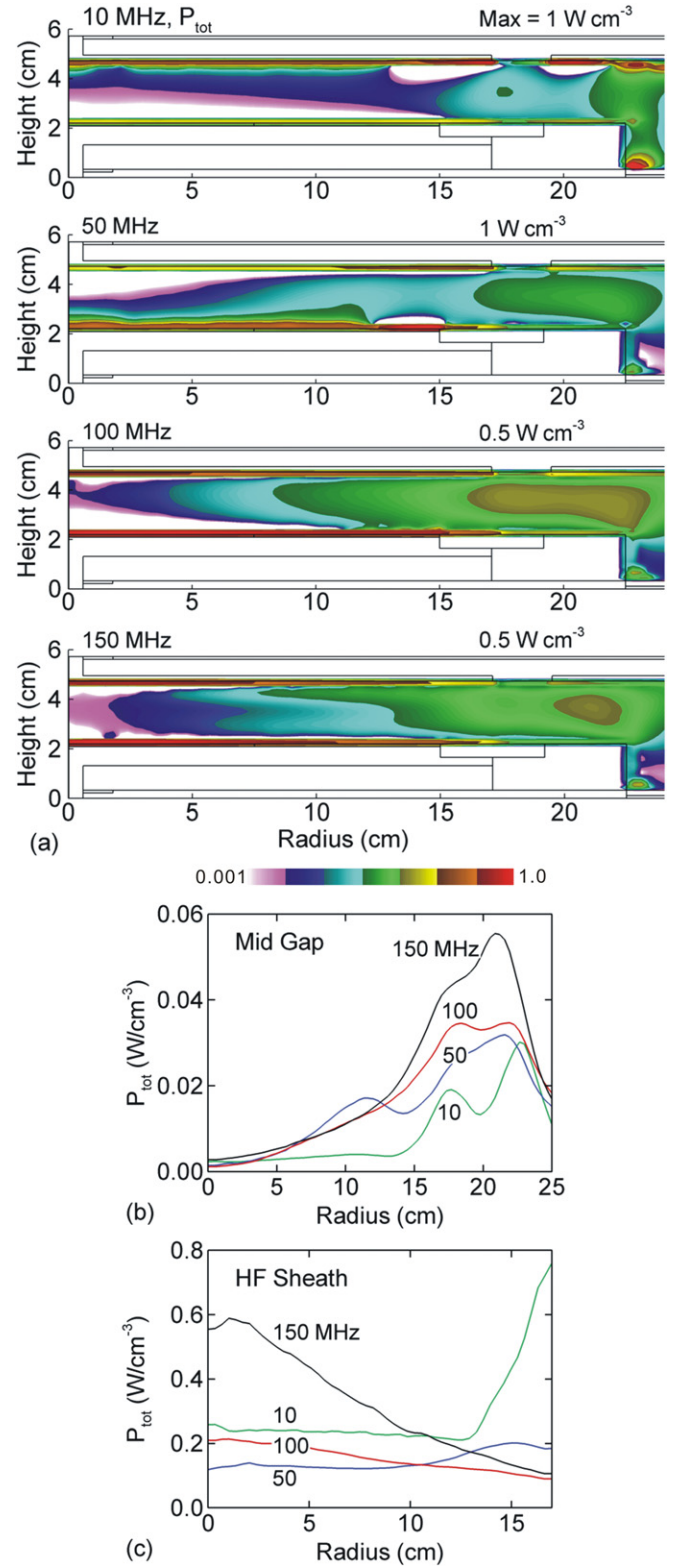
The HF and LF voltage amplitudes were adjusted to maintain constant power at their respective frequencies as the HF is increased. Due to the increase in plasma density, these voltage amplitudes generally decrease with increasing HF. For example, to maintain 300 W, at HF = 10 MHz, the rf amplitude at the HF cable is 125 V, whereas at HF = 150 MHz, the amplitude is 78 V. However, the rf voltage amplitudes are not necessarily linear functions of HF and may depend on the details of the reactor geometry. For example, in this particular geometry, the reactor behaves like a resonator at 50 and 100 MHz, and lower HF voltage amplitudes are required to deposit 300 W (45 V at 50 MHz and 30 V at 100 MHz). The LF voltage amplitude is not a linear function of the HF irrespective of the linearly increasing plasma density. For example, the LF rf voltage amplitude increases from 148 V at HF = 10 MHz to 193 V at HF = 100 MHz and then decreases to 169 V at HF = 150 MHz. This variation in the LF amplitude results from two opposing trends. The first is the increase in maximum plasma density which should, in principle, produce a decrease in the LF amplitude (for constant power) because the current density increases. However, concurrent to the increase in maximum plasma density, the spatial distribution of current density becomes less uniform, which may require an increase

Figure 6. Magnitude of the radial HF field ($|E_{mr}|$) for the base case conditions (Ar, 50 mTorr, $P_{HF} = P_{LF} = 300$ W, LF = 10 MHz). (*a*) HF = 10, 50, 100, 150 MHz; (*b*) $|E_{mr}|$ as a function of radius at the middle of the gap and (*c*) $|E_{mr}|$ as a function of height at $r = 18$ cm. The range of values in each frame is noted. The $|E_{mr}|$ is a log scale over two decades.
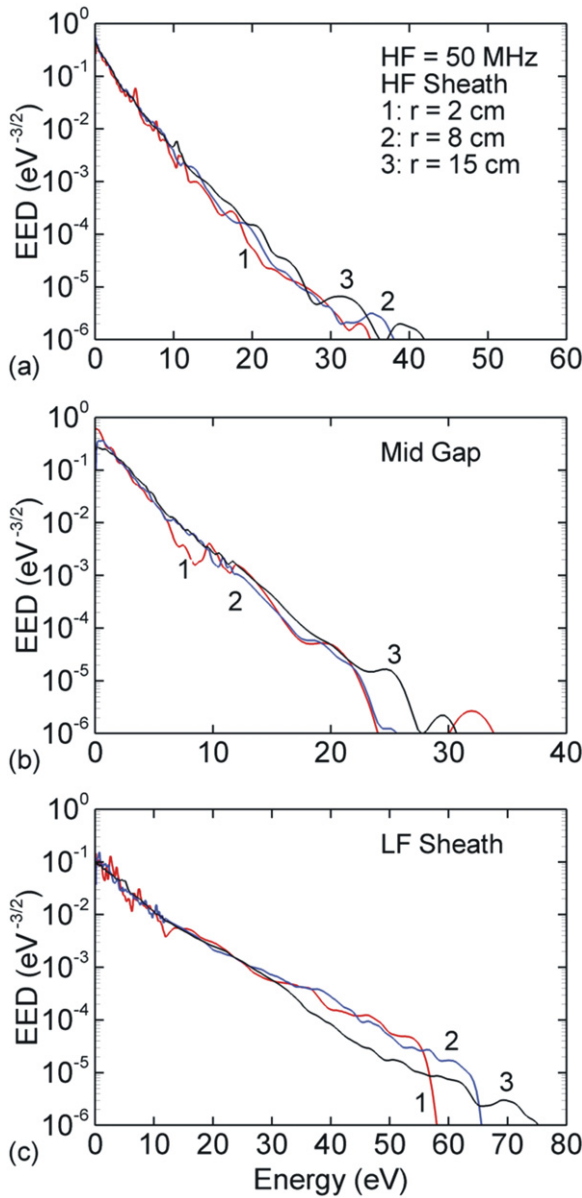
in LF amplitude to maintain the power. The dc bias on the LF electrode generally decreases (becomes less negative) with increasing HF, (from -100 V at HF $= 10$ MHz to -46 V at HF $= 150$ MHz), in agreement with previous studies [22].

Figure 7. Time averaged total power deposition ($P_{tot} = (1/\Delta t) \int \vec{E} \cdot \vec{J} \, dt$) for the base case conditions (Ar, 50 mTorr, $P_{HF} = P_{LF} = 300$ W, LF = 10 MHz). (*a*) HF = 10, 50, 100, 150 MHz; (*b*) P_{tot} as a function of radius at the middle of the gap ($z = 3.5$ cm) and (*c*) P_{tot} as a function of radius at the edge of the HF sheath ($z = 4.56$ cm). The maximum value or range of values in each frame of the contour plots is noted where P_{tot} is on a log scale over three decades.
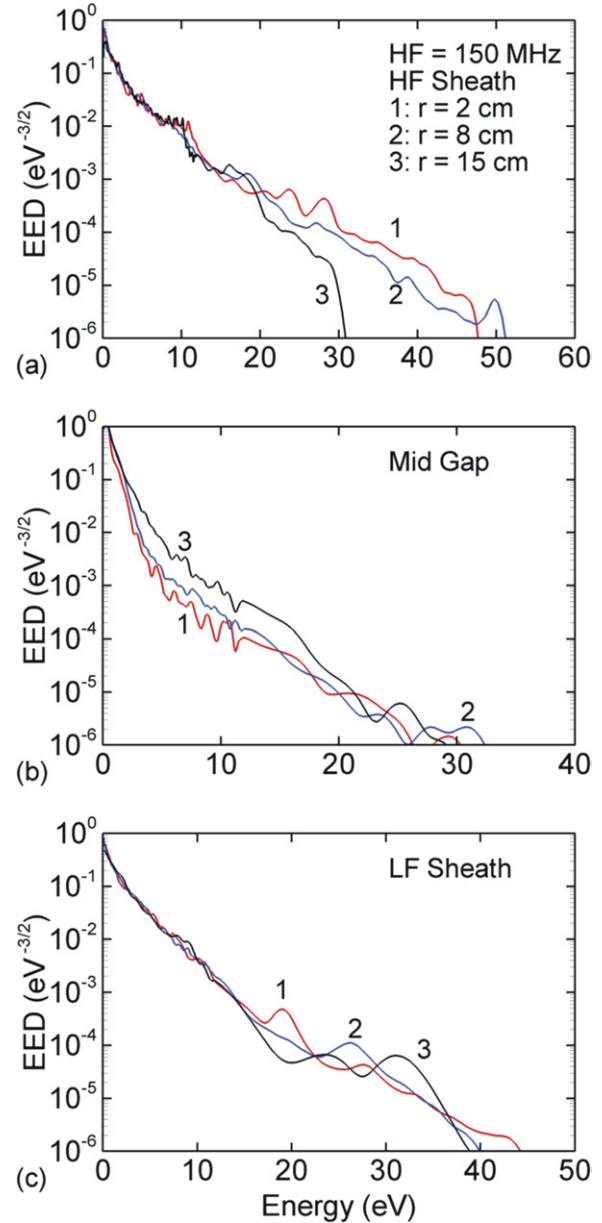
Figure 8. EEDs at different locations in the reactor for the base case conditions (Ar, 50 mTorr, $P_{HF} = P_{LF} = 300$ W, LF = 10 MHz) with HF = 50 MHz. (*a*) In the HF sheath, (*b*) at mid-gap and (*c*) in the LF sheath. (These locations are shown in figure 1(*b*).) Near the edge of the LF electrode, the EEDs in the LF sheath have more prominent tails due to the ES edge enhancement.
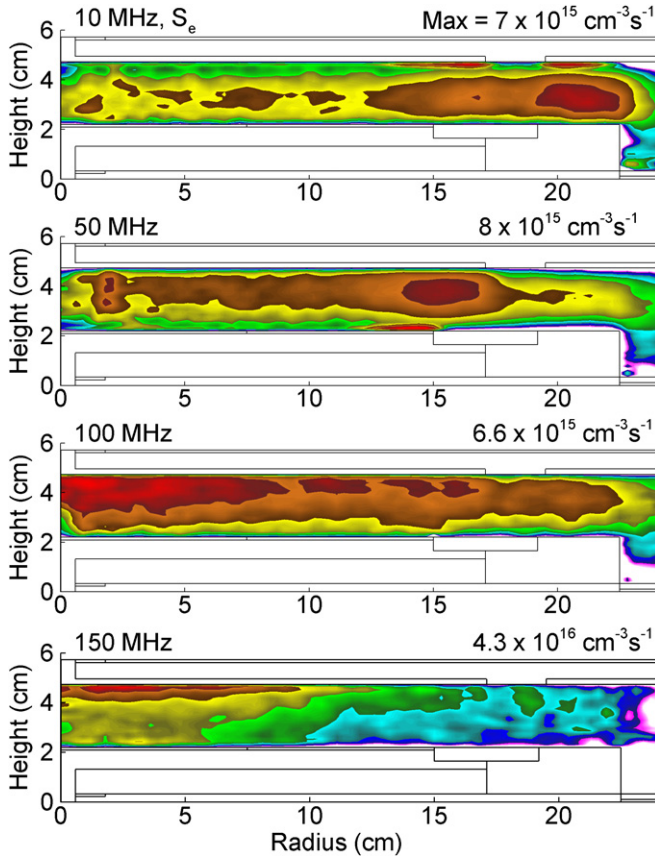
Figure 9. EEDs at different locations in the reactor for the base case conditions (Ar, 50 mTorr, $P_{HF} = P_{LF} = 300$ W, LF = 10 MHz) with HF = 150 MHz. (*a*) In the HF sheath, (*b*) at mid- gap and (*c*) in the LF sheath. (These locations are shown in figure 1(*b*).) Near the center of the reactor, EEDs in the HF sheath have more prominent tails due to the finite wavelength effect which increases sheath heating.
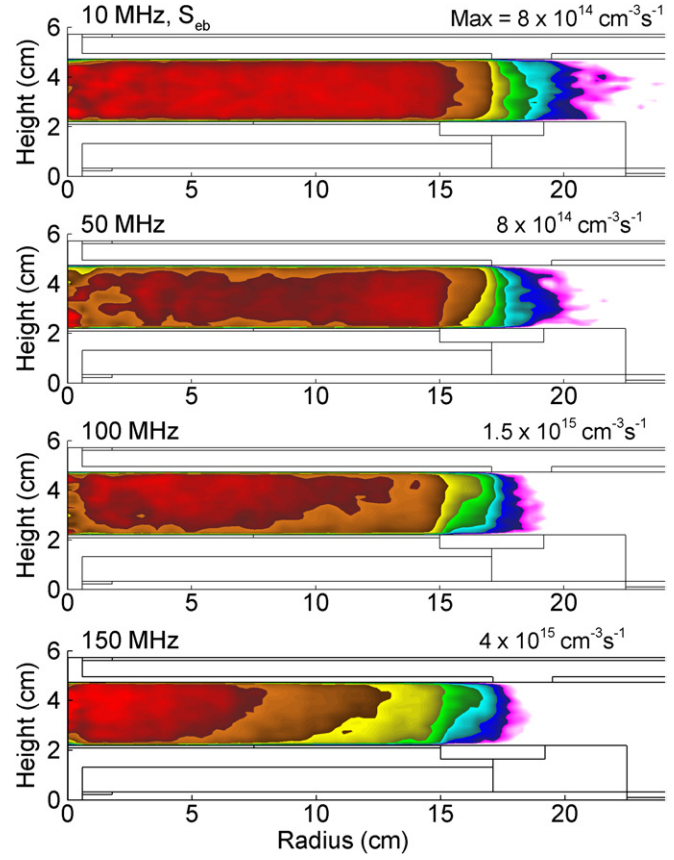
3.3. EEDs and ionization sources

Successful application of DF-CCP tools in semiconductor processing depends on selectively promoting desired plasma chemical reactions and preventing undesirable reactions in order to tailor the reactive fluxes to the substrate. Controlling these fluxes ultimately depends on controlling electron impact reactions with feedstock gases and their fragments. As such, the ability to tailor EEDs is key to this selectivity as EEDs control the generation of radical and ions through electron impact reactions.

The tailoring of EEDs by varying the HF is shown in figures 8 and 9 where EEDs near the center ($r = 2$ cm), middle ($r = 8$ cm) and the edge ($r = 15$ cm) of the electrodes are

plotted for HF = 50 and 150 MHz. EEDs are shown at the edge of the HF sheath ($z = 4.6$ cm), in the middle of the electrode gap ($z = 3.5$ cm) and at the edge of the LF sheath ($z = 2.3$ cm). (These locations are shown in figure 1.) At HF = 50 MHz, the response of the EEDs to electric fields penetrating into the plasma is a small enhancement of the tail of the EED at large radius. This enhancement in the tail of the EED is most prominent near the LF sheath due to the more dominant ES edge effect at LF. The EEDs are nearly uniform as a function of radius across the HF sheath. Regardless of the locations, the EEDs are typically single-temperature distributions.

Figure 10. Time averaged electron impact ionization source (S_e) by bulk electrons for the base case conditions (Ar, 50 mTorr, $P_{HF} = P_{LF} = 300$ W, LF = 10 MHz) and HF of 10, 50, 100 and 150 MHz. The maximum value in each frame is noted. S_e is a log scale over two decades. With increasing HF, the maximum of S_e shifts toward the HF electrode due to enhanced sheath heating and toward the center of the due to the finite wavelength effect.

Figure 11. Time averaged ionization source (S_{eb}) by secondary electrons for the base case conditions (Ar, 50 mTorr, $P_{HF} = P_{LF} = 300$ W, LF = 10 MHz) and HF of 10, 50, 100 and 150 MHz. The maximum value in each frame is noted. S_{eb} is a log scale over two decades. The distribution of S_{eb} follows the ion fluxes which produce the secondary electrons. S_{eb} accounts for less than 10% of the total ionization.

With increasing HF, there is a transition from a single-temperature to a two-temperature EED. This transition likely results from the more efficient sheath heating at higher HF, which populates the high energy tail [23]. At 150 MHz, the tails of EEDs in the HF sheath are lifted in the center and middle of the reactor compared with the edge. This lifting of the tails of the EEDs results from the finite wavelength effect which produces a larger electric filed at the HF sheath in the center of the reactor compared with the edge. With the skin depth being shorter than the electrode separation at 150 MHz, the penetration of HF wave into the bulk plasma is weakened and the tails of EEDs at mid-gap in the center of the plasma are not enhanced. In fact, the EEDs in the bulk plasma near the edge of the HF electrode are lifted in the range 0–20 eV, an effect most likely resulting from enhanced Ohmic heating in the low electron density region. Recall that the electric field in the LF sheath is modulated at the HF. A consequence of the electron heating by the HF field, which is center peaked, and heating by the LF field, which is edge peaked, is a fairly uniform EED along the LF sheath.

The electron impact ionization sources by bulk electrons (S_e) are shown in figure 10 and the ionization sources by beam electrons (S_{eb}) are shown in figure 11 for HF = 10–150 MHz.

(Beam electrons refer to those electrons produced by secondary emission from the HF and LF electrodes by ion bombardment and which are accelerated in the sheaths.) As the HF increases, there is a systematic shift in the maximum of both S_e and S_{eb} toward the HF electrode and toward the center of the reactor. The shift toward the center of the reactor for S_e results from the constructive interference of the finite wavelength effect which increases the magnitude of the electric fields in the HF sheath and so populates the tails of the EEDs which are most responsible for ionization. The shift upward toward the HF electrode can be attributed to at least two effects—the transition from bulk Ohmic heating to sheath heating as being the dominant source of power and a decrease in the skin depth. At HF = 10 and 50 MHz, Ohmic heating dominates and S_e is maximum in the bulk plasma. With increasing HF, stochastic sheath heating begins to dominate and S_e becomes more localized toward the sheath. This shift in power deposition tends to be self-reinforcing. As the electron density shifts toward the center of the reactor a larger fraction of the power deposition occurs there which, for a fixed total power deposition, reduces the proportion at larger radius. Also, as the tail of the EED is populated at HF and the energy relaxation distances decrease, a larger fraction of the power deposition

occurs near the HF electrode where the electrons are initially accelerated.

The radial dependence of the ionization sources from beam electrons, S_{eb}, largely mirrors that of the ion density. The ion fluxes into the electrodes produce the secondary electrons. The secondary electrons are launched into the bulk plasma with nearly the instantaneous sheath potential, which is modulated by both the HF and LF fields. The maximum energies of the secondary electrons usually exceed hundreds of eV. This produces a mean free path commensurate with the electrode separation, thereby providing fairly uniform ionization as a function of height. Since the amplitude of the HF sheath is typically lower than the LF sheath, the secondary electrons from the HF electrode have lower energies and so are more collisional. They are also more likely to be reflected back into the bulk plasma by the more negative LF sheath, a phenomenon termed *trapping*. Secondary electrons from the LF electrode are more energetic and more likely to be collected by the HF electrode as they are able to climb the negative potential of the smaller HF sheath. The end result is that the secondary electrons produce less than 10% of the total ionization.

The importance of beam ionization compared with the bulk was evaluated by integrating S_{eb} and S_e over the volume of the reactor, and taking the ratio of the integrals, $(S_{eb}/S_e)_v$. The expectation is that $(S_{eb}/S_e)_v$ should decrease as the HF increases. This is because the efficiency of low energy electron heating increases with increasing frequency, thereby increasing S_e, while the dc bias decreases, which should decrease S_{eb}. For these conditions, $(S_{eb}/S_e)_v$ increases from 0.13 at 10 MHz to 0.17 at 150 MHz due in large part to the change in the spatial distribution of the plasma. At LF, a large proportion of the plasma extends beyond the edges of the electrodes and so is outside the region where large sheath potentials will produce energetic beam electrons. (The sheath potentials above the surrounding dielectrics are small compared with over the electrodes.) So the proportion of the total ion flux that produces energetic secondary electrons is small. As the frequency increases, the plasma is nearly totally confined between the electrodes where the sheath potentials are large, and so the majority of the ion flux produces energetic secondary electrons.

4. Plasma properties in Ar/CF$_4$

4.1. Electron and negative ion densities and EM fields

Discharges sustained in Ar/CF$_4$ mixtures behave fundamentally differently from those sustained in pure Ar owing to the electronegativity of CF$_4$. Dissociative attachment of CF$_4$ and its fragments mainly generates F$^-$ and CF$_3^-$. The dominant attachment processes have resonant cross sections which are non-zero between 4.4 and 12 eV and have a peak at about 8 eV of 0.025 Å^2 [24]. Although the rates of attachment are low compared with thermal attaching molecules such as SF$_6$ and Cl$_2$, these processes nevertheless decrease the electron density as they require lower electron energies compared with ionization (having a threshold energy of 16.5 eV). Perhaps more important, the products of these processes, negative ions, can

also affect the spatial distribution of electrons by reshaping the ES potential, which in turn shapes the plasma conductivity. The final outcome is that the effective plasma wavelength and skin depth change in a non-monotonic manner as a function of both frequency and radial position, all of which induce different EM effects.

The electron density and total negative ion density ([M$^-$] = [CF$_3^-$] + [F$^-$]) are shown in figures 12 and 13 for LF = 10 MHz (300 W) and HF = 10–150 MHz (300 W) for Ar/CF$_4$ = 90/10 at 50 mTorr. Both the electron density and negative ion density increase with increasing HF due to more efficient electron heating and less power dissipation by ion acceleration. (Although the peak electron density decreases from 50 to 100 MHz due to the persistence of an edge effect at 50 MHz, the reactor integrated electron density monotonically increases with increasing HF.) The electronegativity, defined by the reactor average of [M$^-$]/[e], increases from 0.64 at 10 MHz, to 1.1 at 100 MHz, and then decreases to 0.94 at 150 MHz. The total negative ion density transitions from edge high between 10 and 50 MHz to flat at 100 MHz, and to center high at 150 MHz. With increasing HF, the electron density transitions from edge high between 10 and 50 MHz to center-and-edge high at 100 MHz and finally to having a maximum at mid-radius at 150 MHz. In comparison, [e] is center peaked in pure Ar discharges at HF = 150 MHz. This outward shift of the peak electron density with increasing fraction of electronegative gases was also observed by Rauf *et al* [11]. For example, they found that the electron density transitions from being center high in pure Ar discharges to being maximum at mid-radius for discharges sustained in Ar/SF$_6$ = 95/5 (160 MHz, 500 W, 50 mTorr).
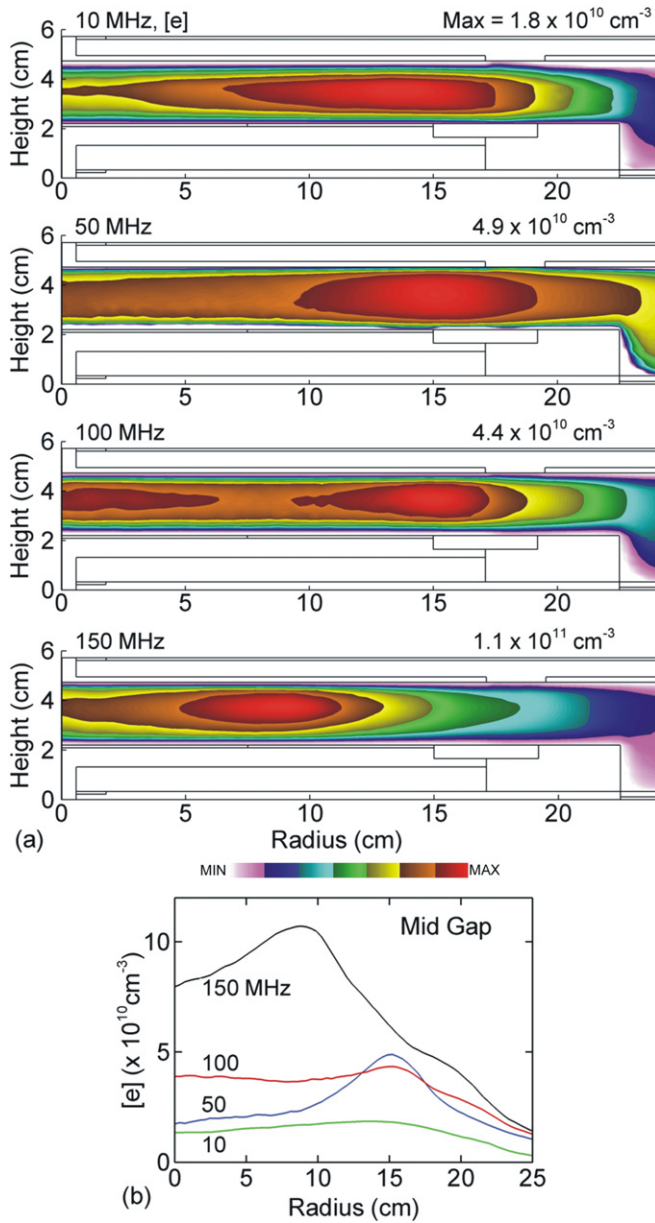
Negative ions are heavy and relatively cool, and so cannot climb the ambipolar potential barrier or sheath potential to reach the electrodes. As a result, negative ions are confined to the electropositive core of the plasma. As the electronegativity of the core of the plasma increases, the plasma potential flattens [25]. This flattening of the potential allows for a more uniform axial distribution of the electron density. Although the maximum values of electron density with increasing HF are smaller than those in discharges in pure argon, the effective plasma quarter wavelengths are still commensurate with the electrode diameter, as shown in figure 14. Correspondingly the HF electric field transitions from edge peaked at 10–50 MHz to being center peaked at frequencies exceeding 100 MHz, also shown in figure 14.

4.2. Electron energy distributions

EEDs for Ar/CF$_4$ = 90/10 are shown at the edge of the HF sheath, mid-gap and the edge of the LF sheath at different radii in figure 15 for 50 MHz and figure 16 for 150 MHz. Similar to the trends in pure Ar, the EEDs transition from single-temperature at 50 MHz to being two-temperature at 150 MHz. This transition is due, in part, to the similarity in the radial profiles of the electric field in the HF sheath in pure Ar and Ar/CF$_4$ = 90/10.

The EEDs at 50 MHz near the HF sheath and mid-gap are essentially the same as a function of radius, with the tail of the
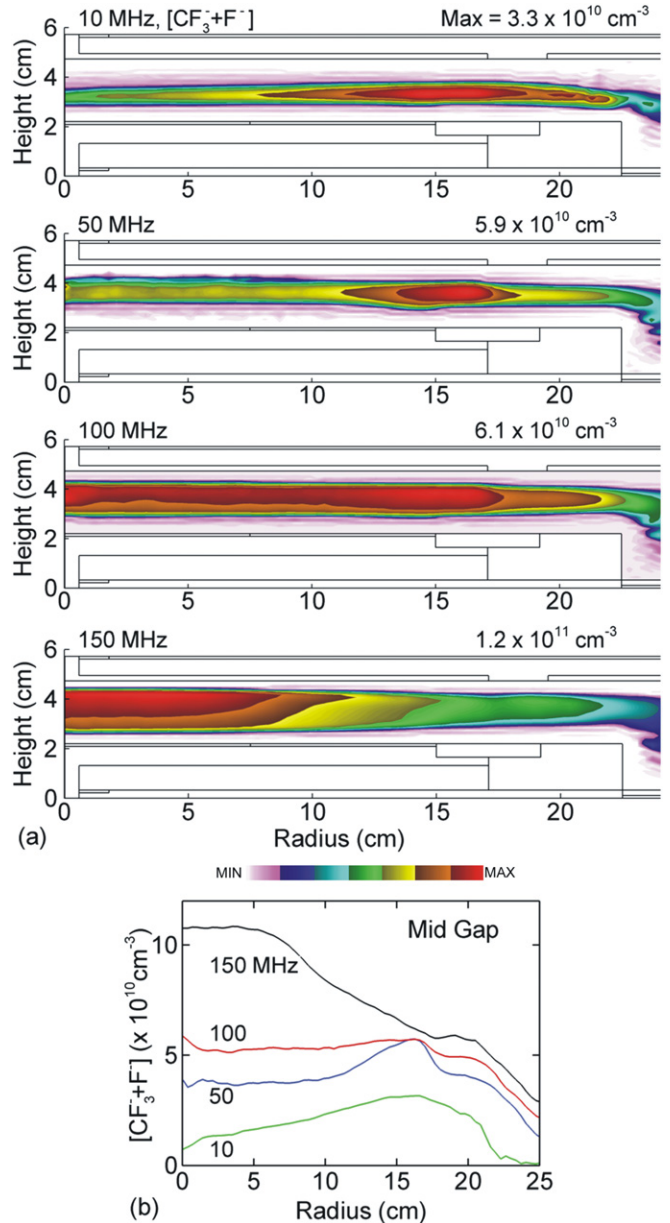
Figure 12. Time averaged electron density ([e]) for
Ar/CF$_4$ = 90/10. (*a*) HF = 10, 50, 100, 150 MHz and (*b*) [e] as a
function of radius at mid-gap. The conditions are otherwise the same
as the base case (50 mTorr, $P_{HF} = P_{LF} = 300$ W, LF = 10 MHz).
The maximum value or range of values in each frame is noted. [e] is
on a linear scale. With increasing HF, the [e] transitions from edge
high between 10 and 50 MHz to center-and-edge high at 100 MHz
and to mid-radius high at 150 MHz.

Figure 13. Time averaged total negative ion density ([CF$_3^-$] + [F$^-$])
for Ar/CF$_4$ = 90/10. (*a*) HF = 10, 50, 100, 150 MHz and
(*b*) ([CF$_3^-$] + [F$^-$]) as a function of radius at mid-gap. The maximum
value or range of values in each frame is noted. ([CF$_3^-$] + [F$^-$]) is
on a linear scale. With increasing HF, the maximum of the total
negative ion density shifts toward the center of the reactor due to a
shift in the EEDs which favor attachment.

EED raised toward the center of the reactor. This occurs even
though the electric field in the sheath is not yet peaked at the
center of the reactor. From the edge to the center of the plasma,
the electron density decreases by a factor of 4 along the HF
sheath. So the lifting of the tails of the EED likely results from
enhanced Ohmic heating in the center of the reactor where the
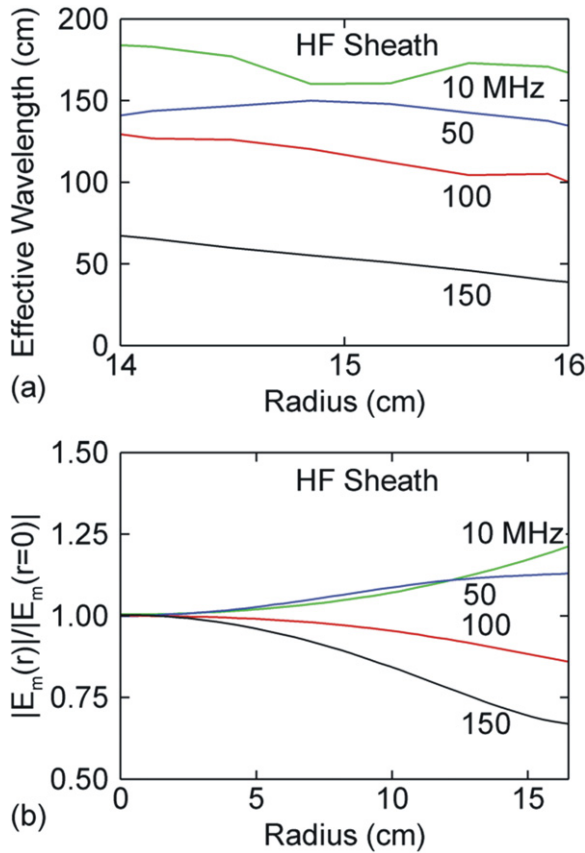electron density is relatively low.

In the bulk plasma at 50 MHz, the electron density
decreases by about a factor of 2 from the edge to the center
of the reactor, compared with a decrease of a factor of 4 at
the edge of the sheath. Therefore, at least on a relative basis,

Ohmic heating in the center of the reactor compared with the
edge is less important in the bulk plasma compared near the HF
sheath. The compromise between less Ohmic heating in the
center and larger electric fields in the sheath near the edge of the
electrode produces nearly uniform EEDs in the bulk plasma.
At the LF sheath, the compromise between Ohmic and sheath
heating is such that the tails of EEDs are most prominent at
mid-radius of the reactor (figure 15(*c*)).

The EEDs for HF = 150 MHz in Ar/CF$_4$ = 90/10 have
2-temperature shapes. As the electric field in the HF sheath is
center peaked, the tails of EEDs near the HF sheath are lifted in
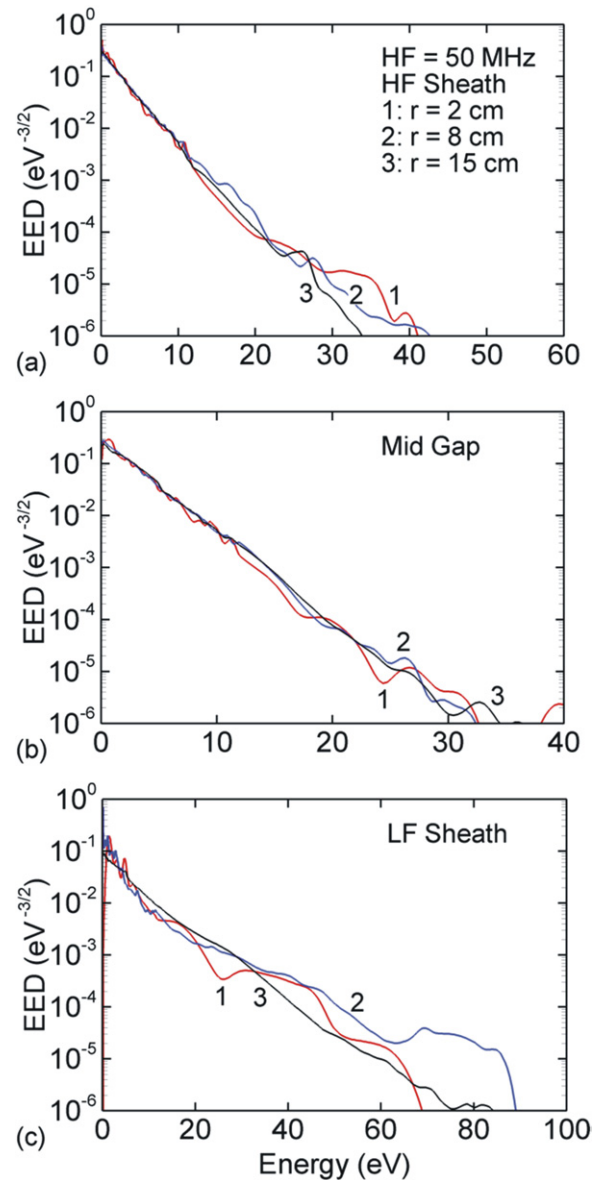the center and middle of the reactor relative to the edge. This

Figure 14. EM properties for Ar/CF$_4$ = 90/10 and
HF = 10–150 MHz. (*a*) Plasma effective wavelength in the HF
sheath, (*b*) magnitude of the HF electric field in the HF sheath
(normalized by the magnitude of the field at the center of the
reactor). The changes in the plasma wavelength and electric field as
a function of radius are not as dramatic as in pure Ar as the local
electron density largely remains the same or even increases with HF.

lifting of the tail of the EEDs extends into the bulk plasma and
to the LF sheath. This likely indicates a more efficient coupling
of the HF wave through the bulk plasma to the LF sheath due
to the lower plasma density than obtained in pure argon. The
HF wave can either couple to the LF sheath through the low
conductivity region of the bulk plasma near the periphery of the
electrodes or propagate around the reactor as a surface wave
and then couple the LF sheath. For this particular reactor,
we found that the coupling through the bulk plasma is more
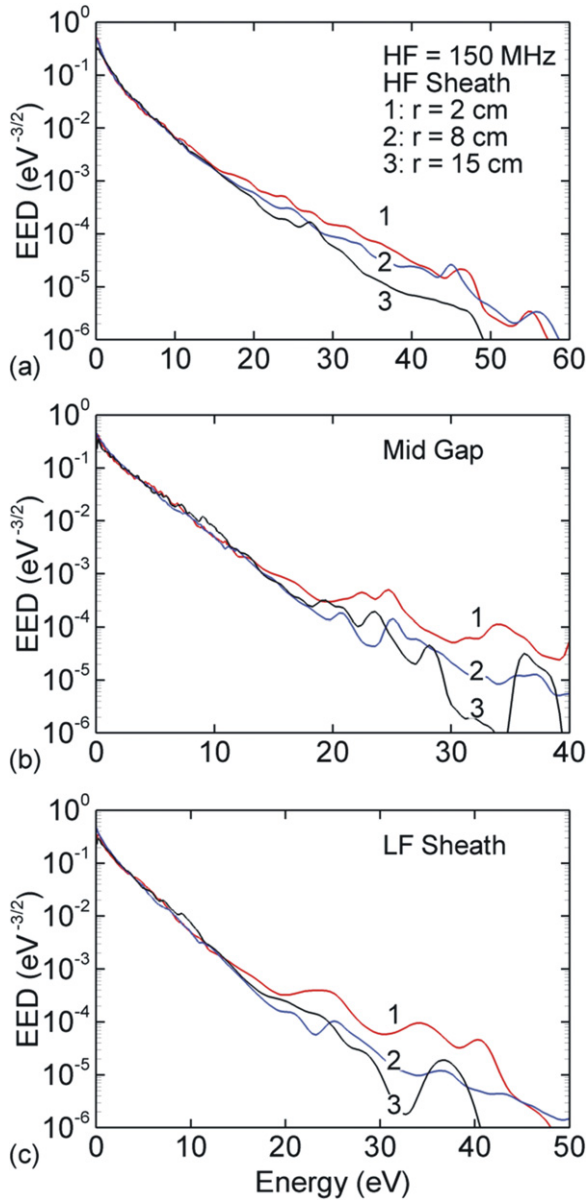important.

4.3. Electronegative effects

Although the trends for propagation of EM fields in Ar/CF$_4$
mixtures are qualitatively the same as in pure Ar, the response
of the plasma and the distribution of plasma density are
different. This results from a correlation between the electron
and negative ion densities which change with HF. For example,
S_e and the source for [M$^-$] are shown in figure 17 for HF = 10–
150 MHz in the axial and radial directions. For HF $\leqslant$ 50 MHz,
S_e is positive throughout the reactor and [M$^-$] is fairly uniform,
which is reflected in the nearly uniform EEDs. Exceeding
100 MHz, sheath heating begins to dominate, lifting the tail of
the EEDs and so electrons are produced closer to the oscillating

Figure 15. EEDs at different locations in the reactor for
Ar/CF$_4$ = 90/10 and HF = 50 MHz. (*a*) In the HF sheath, (*b*) at
mid-gap and (*c*) in the LF sheath. (These locations are shown in
figure 1(*b*).)

HF sheath. Electrons are also produced to a lesser extent closer
to the LF sheath due to more efficient coupling of the HF to the
lower sheath at these lower plasma densities. (S_e near the LF
sheath is typically 3–5 times smaller than near the HF sheath).
Concurrently, there is an increase in the epi-thermal portion
of the EED in the bulk plasma in the center of the reactor due
to the transition to a two-temperature distribution. The EEDs
then better overlap the dissociative attachment cross sections
which increases the rate of attachment sufficiently that the net
source by bulk electrons is negative in the center of the plasma.
The [M$^-$] therefore shifts toward the center of the reactor. The
flatter plasma potential also reduces the magnitude of the bulk
electric field and so the amount of Ohmic heating decreases.
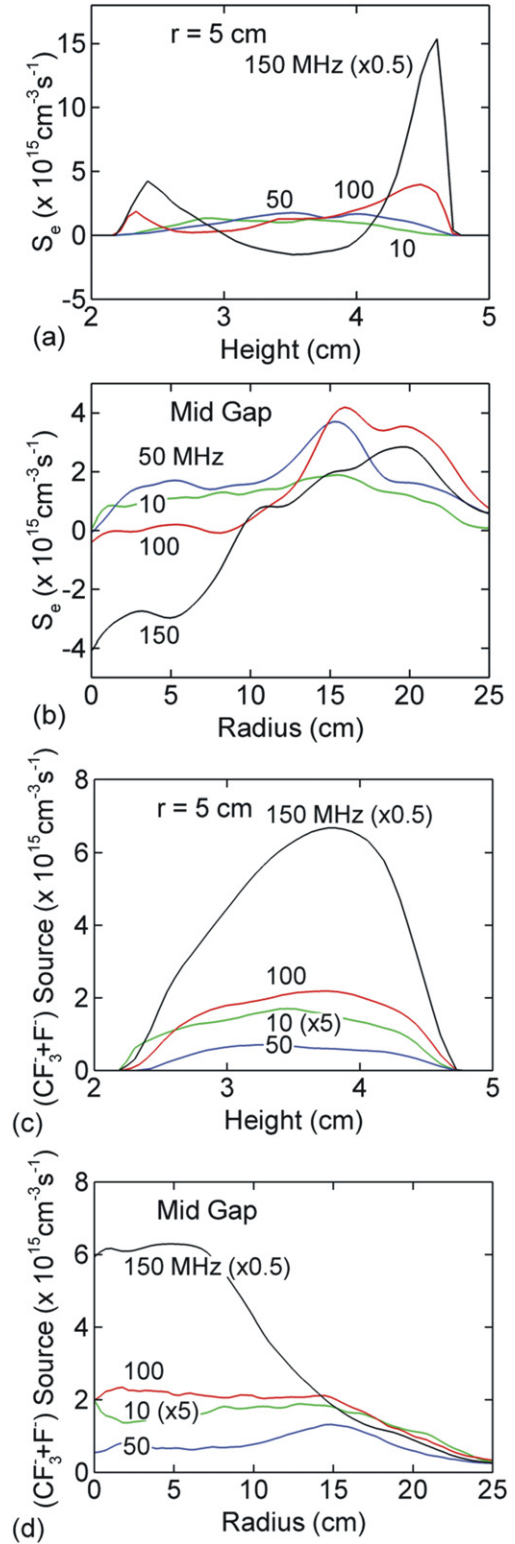
The compromise between the positive S_e near the HF and
LF sheath and the negative S_e in the bulk plasma (all in the

Figure 16. EEDs at different locations in the reactor for Ar/CF$_4$ = 90/10 and HF = 150 MHz. (*a*) In the HF sheath, (*b*) at mid-gap and (*c*) in the LF sheath. (These locations are shown in figure 1(*b*).)
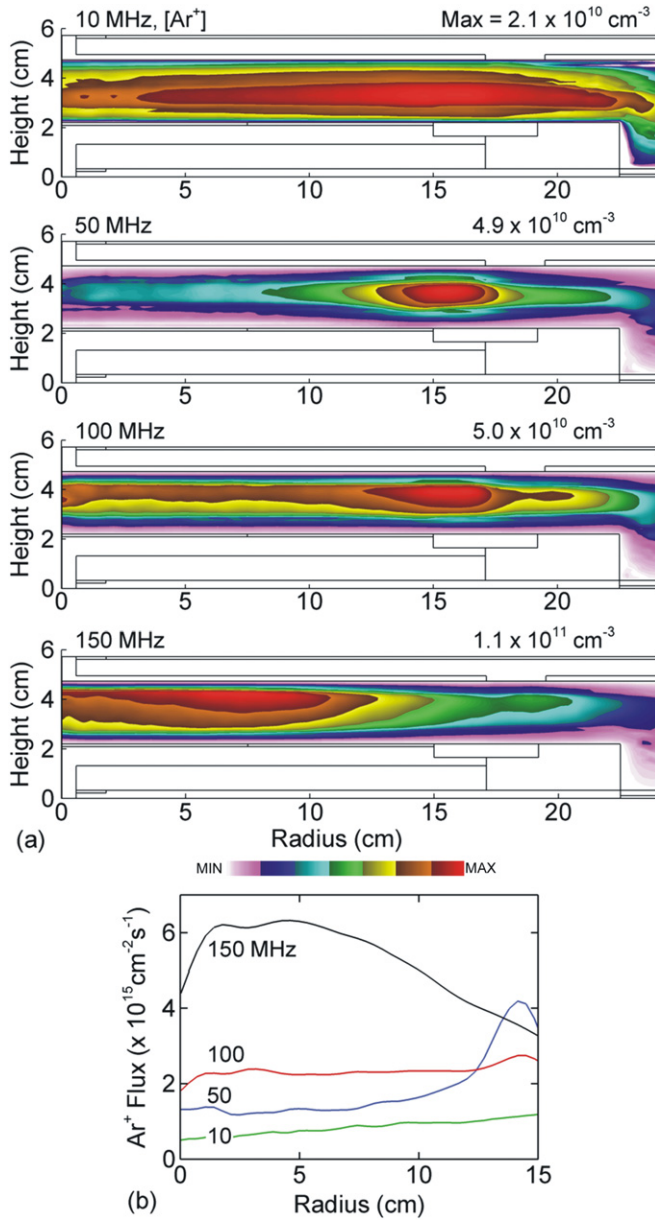
center of the reactor) is partly responsible for the electron density being peaked at mid-electrode at 150 MHz. This shift in electron density is also partly facilitated by the confinement of negative ions in the center of the reactor, which flattens the local plasma potential and enables electrons to diffuse or drift to the periphery of the reactor.

Beam electrons emitted from the powered electrodes are launched into the bulk plasma with essentially the instantaneous sheath potential. So these beam electrons are not particularly efficient at producing dissociative attachment which has low energy resonant cross sections. As such, the ionization source by beam electrons (S_{eb}) is positive throughout the reactor for all frequencies and accounts for 10–15% of the total ionization. The radial profile of S_{eb} largely mirrors that of the total ion fluxes onto the wafer and

Figure 17. Source functions for Ar/CF$_4$ = 90/10 and HF = 10–150 MHz. The conditions are otherwise same as the base case (50 mTorr, P_{HF} = P_{LF} = 300 W, LF = 10 MHz). (*a*) Electron impact ionization source by bulk electrons as a function of height at r = 5 cm and (*b*) as a function of radius at mid-gap. (*c*) Source function for total negative ion production as a function of height at r = 5 cm and (*d*) as a function of radius at mid-gap. Exceeding 100 MHz, sheath heating begins to dominate and electrons are produced closer to the oscillating HF sheath. There are net electron losses in the bulk plasma from attachment.
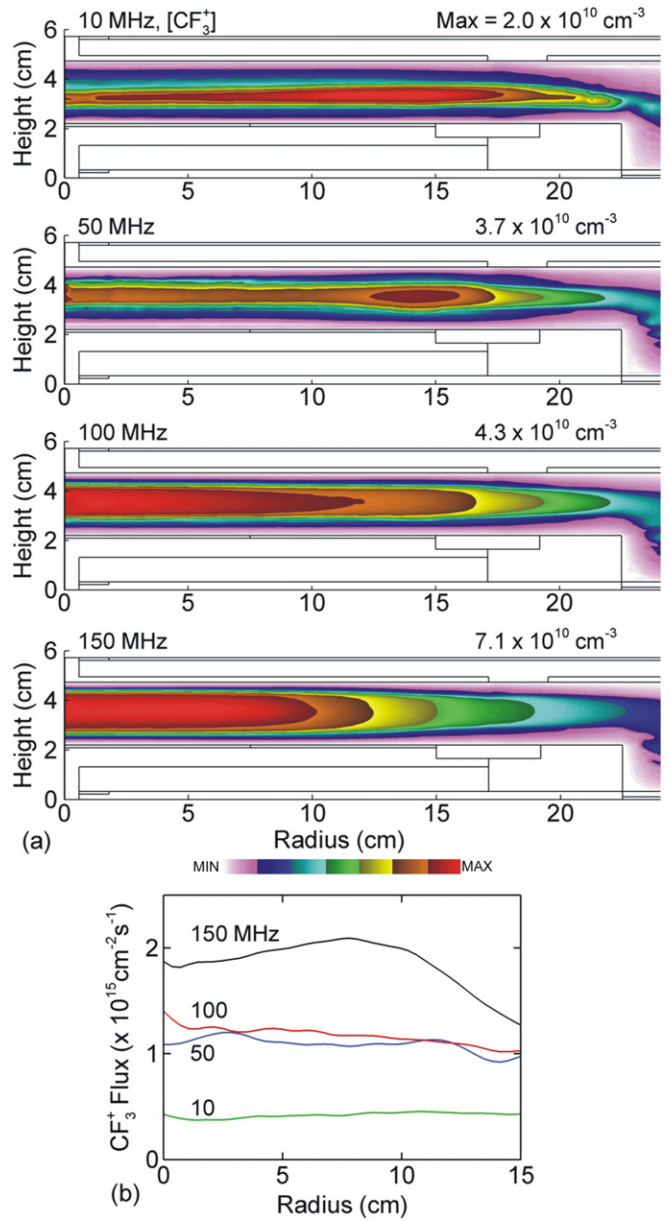
Figure 18. Time averaged Ar^+ density ($[Ar^+]$) for $Ar/CF_4 = 90/10$. (*a*) HF = 10, 50, 100, 150 MHz and (*b*) Ar^+ flux incident onto the wafer. The conditions are otherwise the same as the base case (50 mTorr, $P_{HF} = P_{LF} = 300$ W, LF = 10 MHz). The maximum value or range of values in each frame is noted. $[Ar^+]$ is on a linear scale. $[Ar^+]$ is peaked in the middle of the reactor at 150 MHz with significant contributions from multistep ionization.

Figure 19. Time averaged CF_3^+ density ($[CF_3^+]$) for $Ar/CF_4 = 90/10$. (*a*) HF = 10, 50, 100, 150 MHz and (*b*) CF_3^+ flux incident onto the wafer. The conditions are otherwise same as the base case (50 mTorr, $P_{HF} = P_{LF} = 300$ W, LF = 10 MHz). The maximum value or range of values in each frame is noted. $[CF_3^+]$ is on a linear scale. $[CF_3^+]$ and flux are relatively uniform up to 150 MHz when there is a shift toward the center of the reactor.

transitions from edge high for HF $\leqslant$ 50 MHz to uniform at HF = 100 MHz, to middle high at HF = 150 MHz.

4.4. Ion density, flux and IEADs incident on the wafer

The spatial distributions of ions and their fluxes to the wafer ultimately depend on their sources due to electron impact ionization (or excitation, indirectly) and their subsequent transport and reactions. Since plasma processes such as etching and deposition depend on the relative fluxes of ions, changes in these values as a function of frequency may have an impact on the robustness of the process. For example, the

Ar^+ density is shown in figure 18 for HF = 10–150 MHz and $Ar/CF_4 = 90/10$. With increasing HF, $[Ar^+]$ transitions from being largely uniform at 10 MHz to being edge peaked between 50 and 100 MHz and to being middle peaked at 150 MHz. Since CF_n^+ ions do not charge exchange to Ar, the distribution of Ar^+ in large part reflects its ionization sources, subsequent losses and transport but not additional sources. The volumetric loss of Ar^+ is largely due to charge exchange reactions with CF_4 having a mean free path of 2 cm at 50 mTorr [26]. The edge peak in Ar^+ at 50 MHz corresponds to higher ionization sources due to the extended tails of EEDs near the edge of the LF electrode. The Ar(4s) density largely mirrors the electron
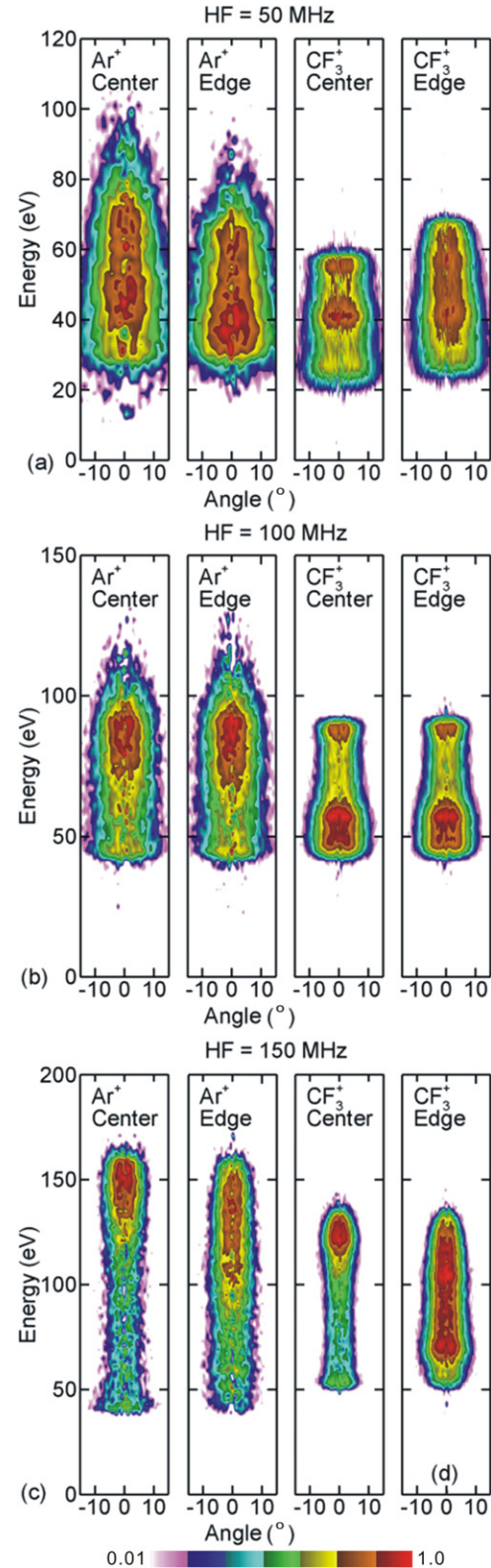
density from 10 to 150 MHz and so multistep ionization also contributes to the edge peak of Ar$^+$. Exceeding 50 MHz, the maximum of [Ar$^+$] shifts toward the HF electrode and the center of the reactor where sheath heating and the finite wavelength effect produces energetic electrons that both ionize Ar and produce Ar(4s) which is then ionized. At 150 MHz, [Ar$^+$] is peaked in the middle of the reactor due in large part to multistep ionization. The Ar$^+$ flux incident on the wafer closely mirrors [Ar$^+$] at all HFs, as shown in figure 18.

The CF$_3^+$ density ([CF$_3^+$]) is shown in figure 19 for HF = 10–150 MHz and Ar/CF$_4$ = 90/10. Ionization of CF$_4$ to generate CF$_3^+$ has a threshold energy of 16.5 eV which is nearly equal to that for Ar$^+$. As a result, the electron impact sources for Ar$^+$ and CF$_3^+$ should be similar. In spite of its higher mass, the mobility of CF$_3^+$ is larger than Ar$^+$ in this mixture due to the lack of symmetric (or asymmetric) charge exchange with a neutral species having a large density. As a result, the spatial distribution of CF$_3^+$ is generally more uniform than for Ar$^+$, which is reflected in the fluxes to the wafer, also shown in figure 19.

The plasma density at the edge of the pre-sheath, and the magnitudes of the LF and HF components in the lower sheath ultimately, determine the radial uniformity of IEADs onto the wafer. To demonstrate these dependences, we separately collected the IEADs over the center of the wafer (from $r = 0$ to 7.5 cm) and over the outer portion of the wafer (from $r = 7.5$ to 15 cm). The IEADs for Ar$^+$ and CF$_3^+$ are shown in figure 20 for HF = 50, 100 and 150 MHz. At 50 MHz, the IEADs for CF$_3^+$ are more extended in energy on the outer portion of the wafer than at the center. The IEADs for Ar$^+$ have an opposite trend. This is particularly the case for the energy of the peak in the IEAD.

These results are counter-intuitive given that in the absence of EM effects, for constant power the LF amplitude and dc biases should decrease with increasing HF. The observed differences are again explained by changes in the spatial distribution of the plasma which translate into differences in sheath thickness, coupled with subtleties of the responses of ions having different masses. There are also EM resonance effects that do not produce linear variations of voltage amplitudes and dc biases with frequency.

So not only is there a center-to-edge variation in the IEADs but these trends are different for different ions. For example, at 100 MHz, the IEADs are essentially uniform from center-to-edge for a given ion due to the sheath thickness being nearly uniform though there are still significant differences between Ar$^+$ and CF$_3^+$, the former having a broader distribution in energy due to its smaller mass. In contrast, at 150 MHz, the IEADs extend to higher energies compared with 50 and 100 MHz, an effect that can be attributed to two factors. First, at 50 and 100 MHz the chamber behaves like a resonator and a lower HF rf voltage is required to deposit 300 W. Though the dc bias decreases from 50 to 150 MHz (less negative, from −100 to −46 V) due to the increasing electronegativity, the maximum allowable ion energy, $V_{HF} + V_{LF} - V_{DC}$, largely remains the same from 50 to 150 MHz (about 310 eV). Second, the higher plasma density at 150 MHz reduces the LF sheath thickness, thereby reducing the ion transit time across the sheath and

Figure 20. IEADs of Ar$^+$ and CF$_3^+$ incident onto the wafer for Ar/CF$_4$ = 90/10 and HF of (*a*) 50 MHz, (*b*) 100 MHz and (*c*) 150 MHz. The conditions are otherwise same as the base case (50 mTorr, $P_{HF} = P_{LF} = 300$ W, LF = 10 MHz). The IEADs are separately collected over the center of the wafer (from $r = 0$ to 7.5 cm) and over the outer portion of the wafer (from $r = 7.5$ to 15 cm). The IEADs have units of eV^{-1} sr^{-1}. The contours span two decades using a log scale. Non-uniform plasma distributions at 50 and 150 MHz result in center to edge variations in the IEADs.

extending the maximum extent of the IEAD. The likelihood for charge exchange in the sheath also diminishes. The end result is an increase in the ion energies incident on the wafer at 150 MHz. As the plasma density decreases over the outer half of the wafer and the sheath thickness increases, the IEADs of Ar^+ and CF_3^+ are shifted down in energy relative to the center of the wafer.

5. Concluding remarks

The properties of DF-CCP sources sustained in Ar and Ar/CF_4 have been computationally investigated using results from a 2D plasma transport model having a time-domain solution of the full-wave, Maxwell equations to resolve EM and ES effects. Similar to the single frequency CCP, in pure Ar DF-CCPs show the trend of a shift in the peak electron density toward the center of the reactor as the HF increases. With increasing HF, the length of the wave decreases and the phase change along the HF sheath increases. From 10–150 MHz, the phase change diminishes toward the center of the reactor, indicating the formation of standing wave. The radial non-uniformity of the HF field is therefore increased and center peaked for HF exceeding 100 MHz due to constructive interference from this finite wavelength effect. The larger electric field in the HF sheath lifts the tails of EEDs in the center of the reactor, thereby increasing ionization rates and producing a center peaked electron density. The maximum of the ionization source, corresponding to the spatial variations of EEDs, shifts toward the center of the reactor and toward the HF electrode due to the enhanced sheath heating and decreasing energy relaxation distance with increasing HF.

For discharges sustained in $Ar/CF_4 = 90/10$, the electron density transitions from edge high between 10 and 50 MHz to center-and-edge high at 100 MHz and to mid-radius high at 150 MHz. This trend likely results from the increasing electronegative nature of the plasma which flattens the time averaged plasma potential. As in the pure Ar discharge, the EEDs in Ar/CF_4 transition from single-temperature at 50 MHz to a two-temperature distribution at 150 MHz, with tails of EEDs being most prominent near the HF sheath in the center of the reactor. This lifting of the tail of the EED also produces increases in the densities of negative ions and CF_3^+ in the center of the reactor. The peak in electron density at mid-radius partly results from the enhanced attachment losses in the center of the reactor. The Ar^+ density is peaked in the middle of the reactor from the multistep ionization as the Ar(4s) density mirrors the electron density. The plasma non-uniformity at 50 and 150 MHz translates to the non-uniformity of ion fluxes and IEADs incident on the wafer.

References

[1] Tsai W, Mueller G, Lindquist R, Frazier B and Vahedi V 1996 *J. Vac. Sci. Technol.* B **14** 3276
[2] Georgieva V and Bogaerts A 2005 *J. Appl. Phys.* **98** 023308
[3] Kitajima T, Takeo Y, Petrovic Z Lj and Makabe T 2000 *Appl. Phys. Lett.* **77** 489
[4] Tong L Z and Nanbu K 2006 *Europhys. Lett.* **75** 63
[5] Chabert P 2007 *J. Phys. D: Appl. Phys.* **40** R63
[6] Lieberman M A, Booth J P, Chabert P, Rax J M and Turner M M 2002 *Plasma Sources Sci. Technol.* **11** 283
[7] Perret A, Chabert P, Booth J P, Jolly J, Guillon J and Auvray Ph 2003 *Appl. Phys. Lett.* **83** 243
[8] Hebner G A, Barnat E V, Miller P A, Paterson A M and Holland J P 2006 *Plasma Sources Sci. Technol.* **15** 879
[9] Miller P A, Barnat E V, Hebner G A, Paterson A M and Holland J P 2006 *Plasma Sources Sci. Technol.* **15** 889
[10] Lee I, Graves D B, and Lieberman M A 2008 *Plasma Sources Sci. Technol.* **17** 015018
[11] Rauf S, Bera K and Collins K 2008 *Plasma Sources Sci. Technol.* **17** 035003
[12] Yang Y and Kushner M J 2010 *Plasma Sources Sci. Technol.* **19** 055012
[13] Kushner M J 2009 *J. Phys. D: Appl. Phys.* **42** 194013
[14] Lu J and Kushner M J 2001 *J. Vac. Sci. Technol.* A **19** 2652
[15] Yee K S 1966 *IEEE Trans. Antennas Propag.* **AP-14** 302
[16] Maloney J G, Smith G S and Scott W R 1990 *IEEE Trans. Antennas Propag.* **38** 1059
[17] Maloney J G, Shlager K L and Smith G S 1994 *IEEE Trans. Antennas Propag.* **42** 289
[18] Mur G 1981 *IEEE Trans. Electromagn. Compat.* **EMC-23** 377
[19] Yang Y, Chen R S and Yung K N 2006 *Microw. Opt. Technol. Lett.* **48** 1619
[20] Rauf S and Kushner M J 1997 *J. Appl. Phys.* **82** 2805
[21] Balannis C A 1989 *Advanced Engineering Electromagnetics* (New York: Wiley) p 149
[22] Rauf S and Kushner M J 1999 *IEEE Trans. Plasma Sci.* **27** 1329
[23] Abdel-Fattah E and Sugai H 2006 *Appl. Phys. Lett.* **83** 1533
[24] Bonham R A 1994 *Japan. J. Appl. Phys. Part 1* **33** 4157
[25] Lichtenberg A J, Vahedi V, Lieberman M A and Rognlien T 1994 *J. Appl. Phys.* **75** 2339
[26] Fisher E R, Weber M E and Armentrout P B 1990 *J. Chem. Phys.* **92** 2296